ACS APPLIED MATERIALS & INTERFACES

Research Article

www.acsami.org

Friction and Wear Mechanisms of Tungsten–Carbon Systems: A Comparison of Dry and Lubricated Conditions

Pantcho Stoyanov,*[,†,‡,§] Priska Stemmer,[‖] Tommi T. Järvi,[†,‡,§] Rolf Merz,[⊥] Pedro A. Romero,[†,‡,§] Matthias Scherge,[†,‡] Michael Kopnarski,[⊥] Michael Moseler,[†,‡,#] Alfons Fischer,[‖] and Martin Dienwiebel[†,§,‡]

[†]KIT-IWM MicroTribology Center μTC, P.O. Box 41 01 03, 76229 Karlsruhe, Germany

[‡]Fraunhofer-Institute for Mechanics of Materials IWM, Wöhlerstrasse 11, 79108 Freiburg, Germany

[§]Institute for Applied Materials IAM, Karlsruhe Institute of Technology, Kaiserstraße 12, 76131 Karlsruhe, Germany

[‖]University Duisburg-Essen - Institute of Product Engineering, Lotharstrasse 1, 47057 Duisburg, Germany

[⊥]IFOS-Institute für Oberflächen- und Schichtanalytik GmbH, Trippstadter Strasse 120, 67663 Kaiserslautern, Germany

[#]Freiburg Materials Research Center, University of Freiburg, Stefan-Meier-Strasse 21, 79104 Freiburg, Germany

ABSTRACT: The unfolding of a sheared mechanically mixed third-body (TB) in tungsten/tungsten carbide sliding systems is studied using a combination of experiments and simulations. Experimentally, the topographical evolution and the friction response, for both dry and lubricated sliding, are investigated using an online tribometer. Ex situ X-ray photoelectron spectroscopy, transmission electron microscopy, and cross-sectional focused ion beam analysis of the structural and chemical changes near the surfaces show that dry sliding of tungsten against tungsten carbide results in plastic deformation of the tungsten surface, leading to grain refinement, and the formation of a mechanically mixed layer on the WC counterface. Sliding with hexadecane as a lubricant results in a less pronounced third-body formation due to much lower dissipated frictional power. Molecular dynamics simulations of the sliding couples predict chemical changes near the surface in agreement with the interfacial processes observed experimentally. Finally, online topography measurements demonstrate an excellent correlation between the evolution of the roughness and the frictional resistance during sliding.

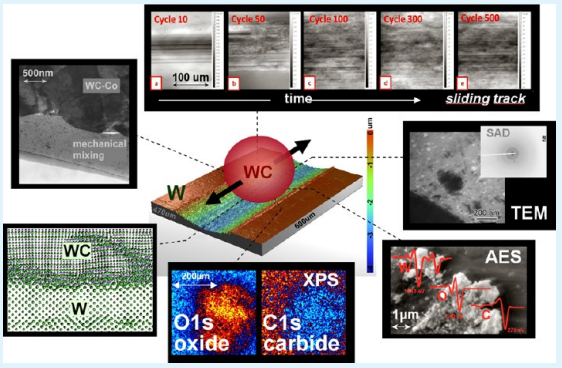

KEYWORDS: *tungsten carbide, third-body, amorphization, mechanical mixing, molecular dynamics, X-ray photoelectron spectroscopy*

1. INTRODUCTION

Many of the mechanisms determining the friction and wear response of sliding couples include dynamic processes within the buried interfaces.[1−8] For metallic alloys, this so-called third-body interface typically consists of mechanically or thermally mixed and deformed material at the surface of each counterface/first-body, transfer films, and debris particles.[9−15] While previous results on pure metals have shown that the formation of 'mixed material' might decrease friction and wear,[16,17] a conclusive correlation between the properties of this layer (e.g., thickness, structural, mechanical, chemical) and the tribological properties has not yet been found, partly due to the missing in situ analyses of the contacting interfaces.

The use of in situ experiments that combine several analytical methods with tribometry has given new insights into sliding contacts.[18−23] A recent review can be found in ref 20. In order to study the interfacial phenomena (e.g., velocity accommodation modes), researchers have often used transparent counterfaces to monitor the contact during sliding of metals and solid lubricant coatings (e.g., MoS_2 based, diamond-like carbon, etc.).[21,22,24−27] Although in situ methodologies within the contact are ideal for understanding third-body behavior, they confine the material selection of the counterface to a transparent one,[20] which makes it somewhat difficult to study tribological pairs for applications without transparent materials (e.g., cutting tools) and are not able to provide quantitative data on topographical changes and wear rates during sliding.

One approach for understanding interfacial mechanisms without the use of transparent materials is to perform numerical investigations. Compared to in situ experiments with transparent counterfaces, molecular dynamic (MD) simulations offer great additional information because they provide details on structural and chemical changes during sliding on the atomic level. Early studies have shown how Lennard-Jones potentials can be used for amorphous and crystalline systems to demonstrate structural changes of sliding contacts (i.e., material

Received: March 19, 2013
Accepted: June 11, 2013
Published: June 11, 2013

   dx.doi.org/10.1021/am4010094 | ACS Appl. Mater. Interfaces 2013, 5, 6123−6135

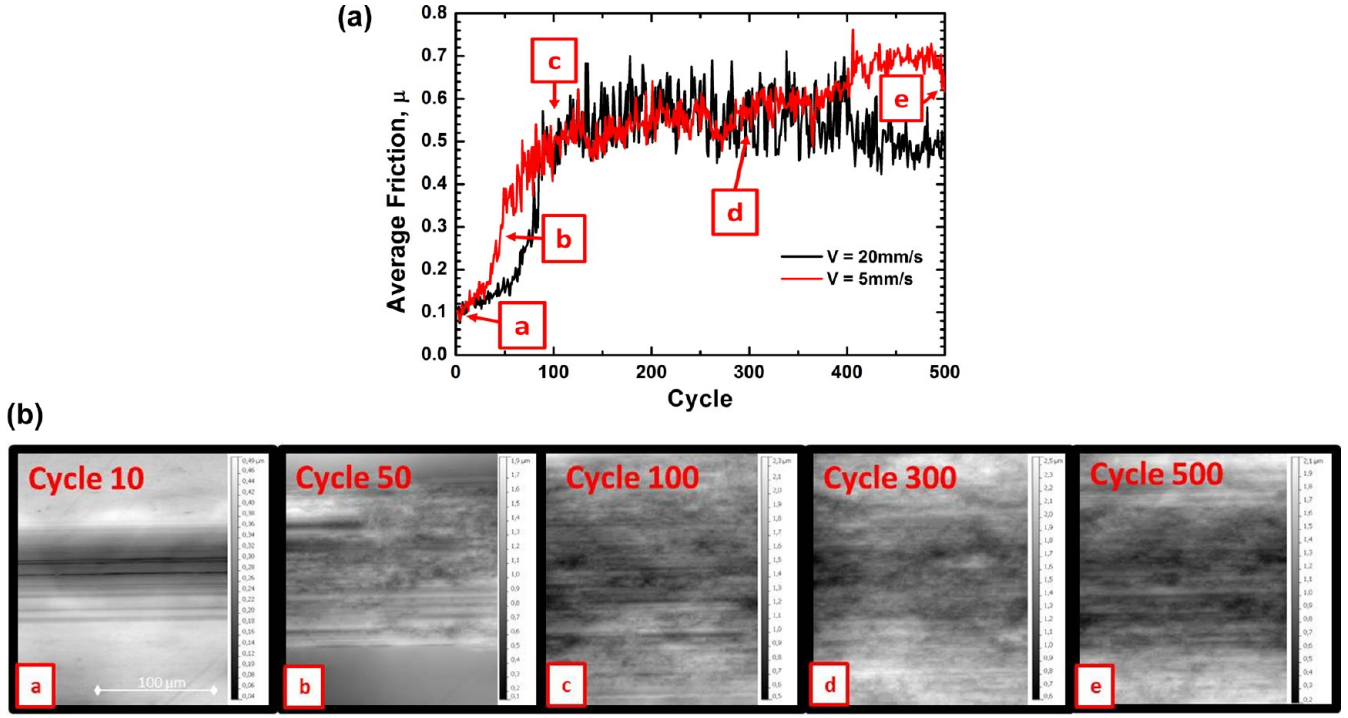

Figure 1. (a) Friction coefficients vs cycle for dry sliding using sliding velocities of 5 and 20 mm/s. The error in the coefficient of friction between two experiments with the same sliding conditions is less than 0.15 (i.e., 0.03 during the running-in period). (b) Topography images of the sliding track (left to right) are obtained using the DHM and are shown below the plot for the 5 mm/s.

transfer, plastic deformation, grain refinement, and material mixing).[13,28−30] By this methodology, Rigney and co-workers associated the structural changes to vortices that are generated as a response to high strain rates. However, it is important to realize that these early pioneering studies focused on generic effects using extremely idealized geometries and materials.

Here we present macroscopic tribometry and atomistic simulations with realistic potentials in order to provide a better understanding of the interfacial processes and behavior throughout the sliding of metals (i.e., tungsten) for dry and lubricated conditions. Reciprocating sliding tests are performed using an 'online' tribometer in order to monitor topographical changes. This allows quantitative wear and roughness measurements to be made after each cycle that are correlated to the friction response, at the position of the measurement. In addition, ex situ analysis is performed on the worn surfaces (i.e., plates and counterfaces) using X-ray photoelectron spectroscopy (XPS), atomic force microscopy (AFM), transmission electron microscopy (TEM), and cross-sectional focused ion beam analysis (FIB) of the near-surface region. Finally we perform molecular dynamics simulations with a realistic bond order potential (BOP) for W−C−H systems,[31] which was screened according to the procedure reported in ref 32 in order to improve the prediction of the cohesive forces between low coordinated atoms. The formulation of the bond order potential and the extended cut off screening function including the values of the screening parameters can be found in ref 33.

2. METHODS

2.1. Experiments. An 'online' tribometer is used to study the friction and topographical changes of W against WC under dry and lubricated (i.e., hexadecane) sliding conditions. This instrumentation consists of a force sensor, digital holographic microscope (LyncéeTec SA DHM R2100), and an atomic force microscope (Bruker AXS Microanalysis GmbH, Germany). The force sensor consists of three SKL 1417-IR (Tetra GMBH, Germany) fiber optic sensors (FOS). A 20× objective lens is used with the holographic microscope in order to measure the wear and roughness after each cycle in the case of dry sliding and a 50× immersion lens in the case of lubricated sliding. More details on the tribometer are described in ref 34. The wear depth values, obtained using the holographic images, are used to calculate the wear rate (i.e., depth/sliding distance) and analyzed in terms of cycle number. The wear depth is measured only up to the 80th cycle due to the width of the wear track being larger than the image size for the remaining cycles. The wear rate of the last cycle is also included in the analysis; however, it is calculated using the depth obtained from the confocal microscope at the end of the test after cleaning the sample.

The sliding tests are performed in reciprocating motion with an 80 mm track length. The initial normal load is 3N, and the sliding velocities are 0.2, 1, 5, and 20 mm/s. The friction coefficient is recorded throughout the whole wear track; however, the friction of each cycle reported in this paper represents an average value between the two nearest points to the position of the DHM, which allows a direct comparison between the topographical changes and the friction behavior. Each experimental condition is performed at least two times to observe the consistency of the tests. The error in the coefficient of friction for the dry sliding tests between two experiments is less than 0.15 (i.e., 0.03 during the running-in period) and for the lubricated case less than 0.02.

Sample characterization and ex situ analysis of the worn surfaces is performed using X-ray photoelectron spectroscopy (XPS) (PHI 5000 VersaProbe, Physical Electronics Inc. and an Axis Nova, Kratos Analytical) in order to observe chemical changes at the surfaces and subsurfaces. XPS depth profiles are plotted in terms of sputtering depth, which is estimated based on depth calibrations with SiO_2 and Ta_2O_5 for the PHI VersaProbe and the Axis Nova, respectively. A sputtering time of 10 min can be estimated to be approximately 20 to 30 nm for both instruments. Besides classical small area XPS spectroscopy (i.e., spot size from Ø100 μm down to Ø10 μm), quantitative chemical concentration maps of the surface can be taken in parallel imaging mode by the Axis Nova. Additional information about the concrete binding energies of detected elements can be obtained according the chemical shift of their binding energy, observed

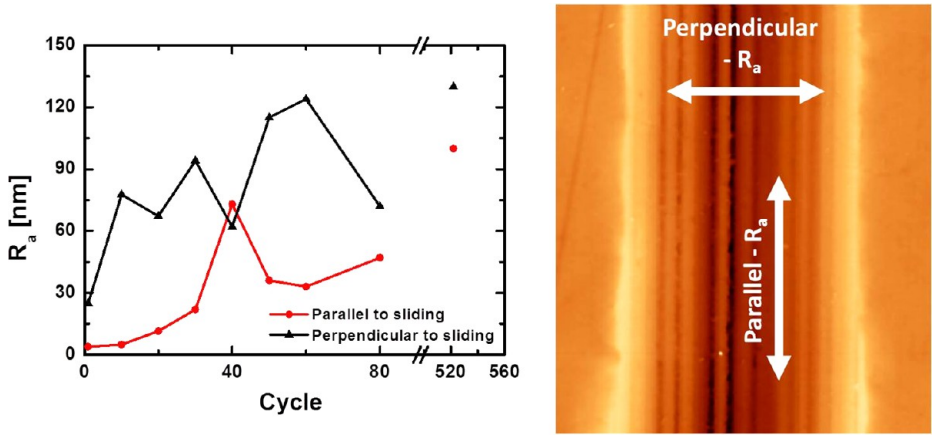

Figure 2. Roughness values obtained using a thin rectangle parallel to the sliding direction and a thin rectangle perpendicular to the sliding direction (right panel). The roughness values obtained from the two directions vs the cycles are shown in the left panel.

in highly resolved chemical state scans. Due to the high surface sensitivity of XPS analysis, with a typical information depth of <3−5 nm, sputter profiling is performed to remove adsorbed films and to access information about deeper regions of the subsurface. Sample cleaning is performed before the analysis by a three phase supersonic bath with cyclohexane, acetone, and isopropyl alcohol. The aim of the cleaning procedure is to remove hexadecane resins to achieve vacuum compatibility as well as disturbing thin contamination layers primarily composed out of aliphatic hydrocarbons.

Debris particles are collected at the end of the sliding experiments and are analyzed using a Transmission electron microscopy (TEM) Philips EM 400 (Eindhoven, Netherlands) and a scanning Auger - Electron Spectrometer (Smart 200, •ULVAC-PHI Inc.). With a similar surface sensitivity as XPS, the highly focused electron beam of the Smart 200, generated by a Schottky-Field Emitter, enables small spot Auger Spectroscopy (i.e., spot sizes down to Ø 35 nm). In addition, this lateral resolution allows for chemical concentration maps by scanning over selected sample areas. In combination with sputter profiling, information about subsurface regions and of the debris particles is accessed. It should be noted that the debris particles for the lubricated sliding conditions are analyzed on aluminum foil. The contribution of aluminum (<10%) and some oxygen from Al_2O_3 have been removed from the results presented in this paper for simplification. In addition, focused ion beam (FIB) (Zeiss XB 1540) cuts on the wear track are performed perpendicular and parallel to the sliding direction to observe microstructural changes near the surface. The images are recorded at a 54° angle, which is taken into consideration for length/size measurements.

The sliding tests for the dry and lubricated case are performed on pure tungsten using a WC-Co sphere as a counterface. The pure tungsten (i.e., 99.9% W) plate is obtained from Goodfellow GmbH in the 'as rolled' condition. WC-Co (94% WC and 6% Co − obtained from Spherotech GmbH) spheres are used as counterfaces for the tribological experiments with a 1.5 mm radius. Further details of the samples used in this study are described elsewhere.[33]

2.2. Simulation. To gain insight into the atomic scale processes of lubricated sliding tribosystems, we employ a bond order potential (BOP) parametrized for tungsten−carbon−hydrogen systems[31] together with a correction to remove the typical bond strength overestimation in BOP potentials.[32] More details on the potential parameters can be found in ref 33. Here, a relatively small scale tribocouple is constructed with the aim of exposing chemical changes between a pair of contacting asperities. To summarize, a model of a tungsten against a tungsten carbide counterbody with atomic level roughness including a hexadecane lubricant at the contact interface is constructed. The tribocouple is then relaxed at 300 K and pressed with a 5 GPa normal pressure prior to the onset of sliding. Subsequently, the contact is sheared with at a velocity of 50 m/s by moving a rigid zone of atoms at the top of the cell relative to a fixed zone at the bottom while maintaining the 5 GPa normal pressure. Additionally, the system contains a heat sink 300 K thermostat above and below the contact interface as well as an augmented mass region at the top as described in ref 35.

3. RESULTS

3.1. Dry Sliding. *3.1.1. Friction and Wear Behavior.* 'Online' tribometry is used to elucidate the third-body behavior throughout the sliding of WC against W. Figure 1 (a) shows the coefficient of friction vs the cycle number for the experiments on tungsten with 5 mm/s[33] and 20 mm/s sliding velocity under dry sliding conditions. Both sliding conditions exhibit similar evolution of the coefficient of friction. As presented in our previous study[33] for the 5 mm/s sliding velocity, the coefficient of friction for the experiments with higher sliding velocities is approximately 0.1 within the first few cycles. Subsequently, it increases up to 0.6 for about 100 cycles where it remains nearly constant for the remainder of the experiment. In addition, the scatter in the friction values for both experiments increases in parallel with the friction coefficient. The depth of the wear tracks is also monitored throughout the test, and the wear rate shows an opposite behavior to the friction coefficient;[33] the wear rate (i.e., calculated using the depth values and the sliding distance) is initially 200 nm/m and decreases to 40 nm/m over 50 cycles where it settles at a nearly constant value.

3.1.2. 'Online' Analysis of the Surface Topography. Topography images of cycles 10, 50, 100, 300, and 500 taken with the DHM are shown in Figure 1 (b). A smooth wear track with narrow grooves (i.e., scratches) parallel to the sliding direction is observed during the running-in period within the first few cycles (i.e., 10th cycle). At cycle 50, the wear track grew significantly wider, and the scratches within the wear track became less obvious. By the 100th cycle, only small parts of the grooves are visible, and the surface is notably rougher. The worn surface grew to be wider than the image size, and therefore it is not possible to observe further changes in the width of the wear track for the remainder of the test. While slight differences in the surface topographies for the remaining cycles are observed, the worn surfaces appear to be of similar roughness.

Average roughness calculations on the wear track are performed from the DHM images at any given cycle. Initially, the average roughness (i.e., obtained using a 20 × 20 μm square) is below 50 nm; however, it increases to 90 nm during

dx.doi.org/10.1021/am4010094 | ACS Appl. Mater. Interfaces 2013, 5, 6123−6135

the first 40 cycles.[33] Subsequently, the average roughness fluctuates between 50 and 130 nm for the remainder of the test. It is also noted that the oscillation in the roughness value decreases with the higher cycle number.

A similar behavior is also observed with roughness values obtained using thin rectangles (20 × 0.6 μm) parallel and perpendicular to the sliding direction, Figure 2. However, differences in the roughness values between the two directions are evident. In the perpendicular direction, the roughness increases instantaneously (i.e., within 10 cycles) to nearly 80 nm, whereas in the parallel direction it took more than four times as long to reach the same roughness value. While the roughness in both directions fluctuates significantly for the remainder of the experiment, the average roughness for most cycles is lower parallel to the sliding direction.

3.1.3. Third-Body Behavior. X-ray photoelectron spectroscopy (XPS) is performed on the worn surfaces and presented elsewhere.[33] The elemental analyses reveal an increase in the oxygen concentration compared to the unworn surface. In addition, the tungsten concentration is lower in the near surface region of the wear track compared to the unworn surface.

Similar to previously reported third-body behavior for solid lubricants,[1] the transferred/mixed material on the WC tip consists of an internal zone (i.e., area in the middle of the contact), entry zones (i.e., located in front of the internal zone[1]), and lateral zones which are located on either side of the internal zone (Figure 3). The average roughness values (R_a) are different between the internal and the entry zone; roughness being nearly double within the entry zone compared to the internal zone (i.e., R_a = 241 nm and R_a = 164 nm, respectively). In addition, the average roughness of the internal zone is similar in magnitude to the one of the wear track at the end of the test.

Elemental analysis of the internal and entry zones is performed using an XPS and shown in Figure 3(a)[33] and (b), respectively. While the tungsten concentration in the two zones is similar, the biggest difference is observed with the carbide concentration; within the internal zone the carbide concentration continuously increases until nearly 40 at.% is reached at a sputter depth of 1000 nm, whereas in the entry zone it remains between 20 and 30 at.% after 100 nm. The opposite behavior is observed with the oxygen concentration, which continuously decreases in the internal zone with respect to the sputter depth. After approximately 20 nm the oxygen concentration in the internal zone is two times lower compared to the concentration in the entry zone.

Figure 4 shows XPS chemical state images of tungsten, oxygen, and carbon at the worn tungsten carbide tips. For each element two chemical states can be distinguished by their chemical shift of the binding energy BE. More specifically, carbon in tungsten carbide ($BE_{C1s/Carbide}$ = 282.8 eV) is separated from the omnipresent organic aliphatic carbon (BE_{C1s} = 285 eV) due to adsorbed layers from environmental influences. In addition, oxygen in tungsten oxide ($BE_{O1s/WO2}$ = 530.6 eV, $BE_{O1s/WO3}$ = 530.8 eV) is separated from mostly organic bounded oxygen ($BE_{O1s/org.}$ = 532.9 eV). While metallic tungsten ($BE_{W4f/metal}$ = 31.4 eV) overlaps tungsten carbide ($BE_{W4f/WC}$ = 31.5 eV), the oxides WO_2 ($BE_{W4f/WO2}$ = 32.8 eV) and WO_3 ($BE_{W4f/WO3}$ = 35.8 eV) can be separated clearly. The XPS chemical state images at the surface are repeated after 125 s, 400 s, and 8000 s of sputtering (2 keV Ar^+) to gain information at different sputter depths, as shown in Figure 4. In addition, the sputtering procedure allows for looking under the typical

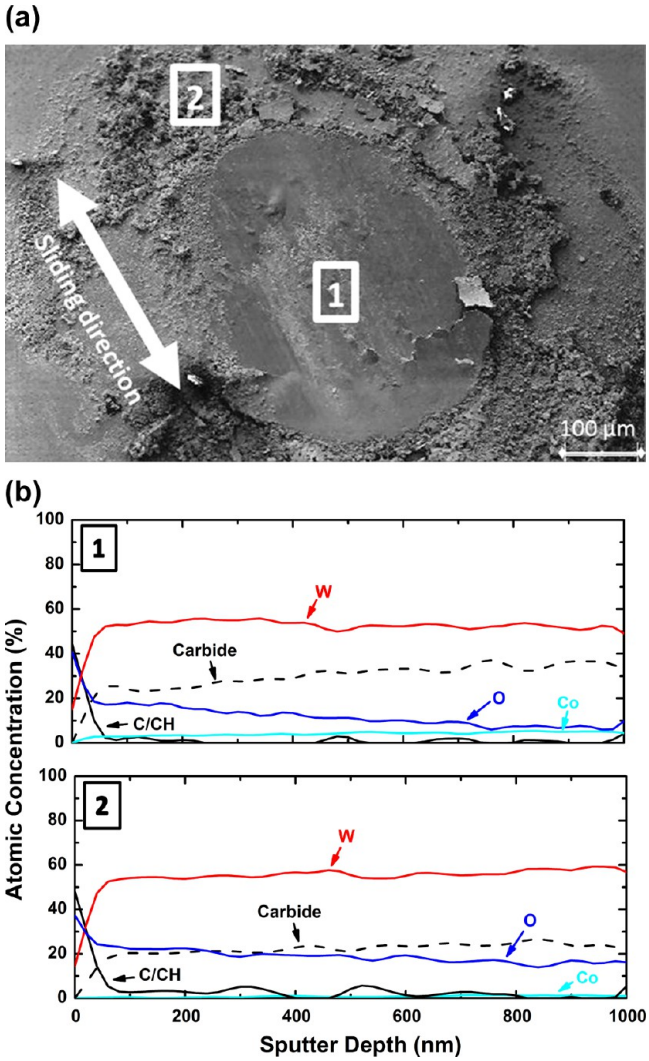

Figure 3. (a) SEM image of the worn WC tip showing the entry and internal zone (i.e., position 1 and position 2) and (b) XPS analysis of the internal zone at position 1 and of the entry zone at position 2.

organic carbon layer, which is present at all samples handled under ambient environmental conditions.

Tungsten (W4f 35.8 eV) bound as WO_3 and oxygen (O1s 530.8 eV) bound in the same WO_3 decrease with respect to the sputter time in the internal zone, as shown in Figure 4. However, tungsten oxide (WO_3) is still present within the contact zone after 8000 s sputtering by 2 keV Ar^+ bombardment. Based on depth calibration measurements with a Ta_2O_5 reference sample, this sputtering time corresponds to a depth of 0.3 μm. The carbon signal of tungsten carbide (C1s 282.8 eV), on the other hand, remains dominant outside of the internal zone throughout the sputter profiling. The chemical state map of the overlapping metallic tungsten and tungsten carbide signals (W4f 31.3 eV) shows a similar behavior to that of the carbon in tungsten carbide. A slightly higher tungsten concentration may be the consequence of metallic tungsten contributions. Oppositely to the decrease of WO_3 during sputtering within the contact zone, the carbide contributions from carbon (C1s 282.8 eV) and tungsten (W4f 31.3 eV) increase. These observations are consistent with the analysis of the depth profiles in Figure 3.

dx.doi.org/10.1021/am4010094 | ACS Appl. Mater. Interfaces 2013, 5, 6123−6135

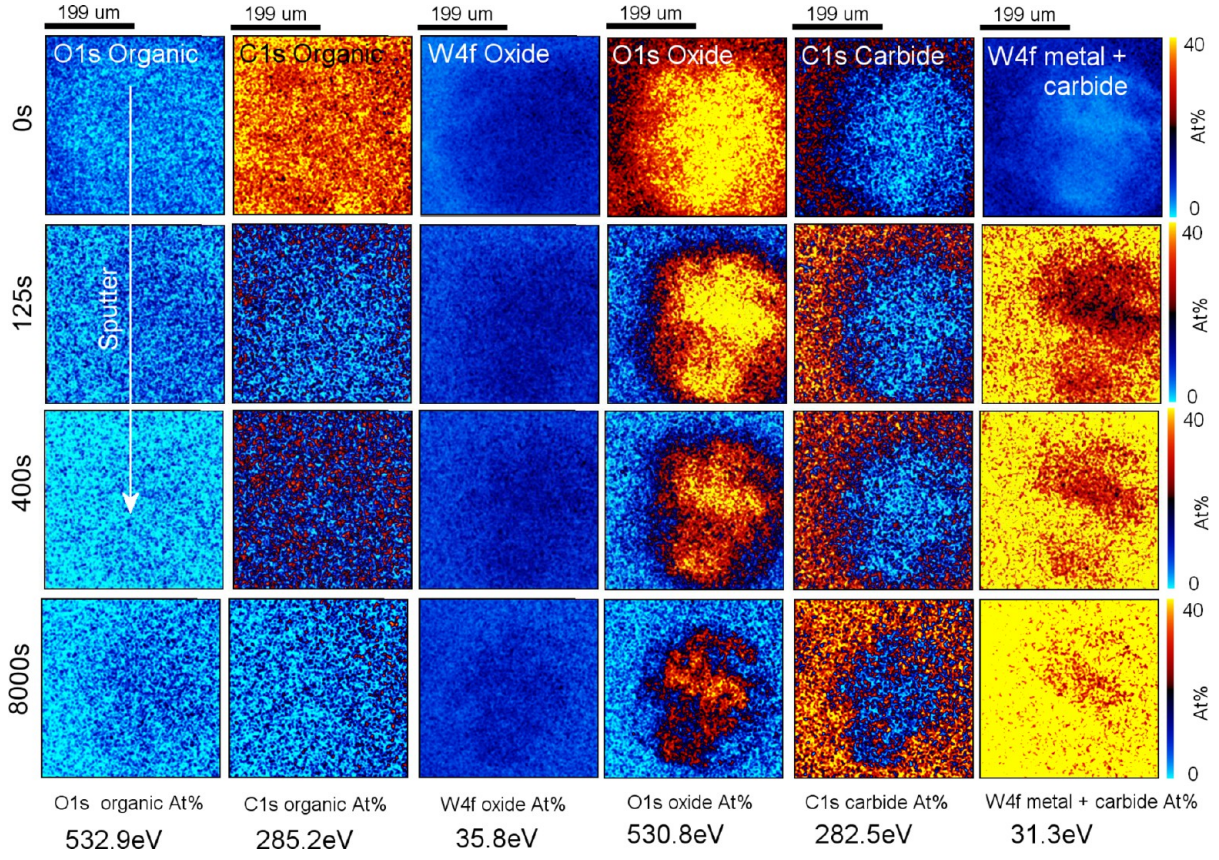

Figure 4. XPS maps of the worn tungsten-carbide surfaces under dry sliding conditions without sputtering, after sputtering for 125 s, after sputtering for 400 s, and after sputtering for 8000 s. The color bar ranges from 0 At-% (blue) to 40 At-% (yellow).

Cross sectional TEM images parallel to the sliding direction of the WC counterface at the end of the test are shown in Figure 5 (a). A third-body is seen on the surface. The thickness of this layer is up to 1.3 μm, and the structure is different compared to the bulk of the WC; nanoparticles are present, which are immersed within an amorphous mixed layer containing a small fraction of nanocrystalline material, Figure 5 (b). According to the XPS chemical state images (Figure 4) up to a sputter time of 8000 s, the mechanically mixed layer (under a very thin adsorbed organic carbon layer) is composed mostly of tungsten oxide with small particles of tungsten and tungsten carbide. The order of magnitude of the sputter depth correspond to the locally observed thickness of the mixed layer in the cross section TEM picture (Figure 5a). As reported in ref 33, cross-sectional FIB cuts of the worn W plate, on the other hand, reveal grain refinement near the surface. Most grains near the contact are smaller than 200 nm in size, and the thickness of the ultrafine grained zone is approximately 700 nm.

Figure 6 shows transmission electron microscopy (TEM) micrographs of debris particles that are collected at the end of the sliding test. Debris particles consist of various shapes and sizes; the size ranged anywhere from a few nanometers to several μm. Larger particles are either flakelike or agglomerates of smaller particles, while the smaller particles exhibit globular or lamellar shapes. The wear particles reveal a crystalline structure and, depending on the type of debris, the electron diffraction pattern identified pure tungsten (W), tungsten carbides (WC, W_2C), tungsten oxides (WOx), and cobalt (Co).

3.1.4. Atomistic Simulations of Dry Contact. Molecular dynamics studies of WC sliding against W were performed in order to understand the underlying atomistic mechanisms leading to the experimentally observed interfacial processes. As previously reported,[33] both atomically flat and atomically rough WC-W nanotribosystems with carbon terminated WC interfaces were constructed. Upon initial sliding of the rough-on-rough tribocouples, the WC asperities plow through the W asperities, and the exposed carbon layer of the WC gradually mixes with the disordered W atoms. As communicated in ref 33, an amorphous tungsten carbide layer was generated which accommodated the sliding motion.

The flat-on-flat simulations revealed that at the onset of sliding the topmost layer of the W surface transfers onto the WC specimen (i.e., bonds to the exposed carbon of the WC surface). Subsequently, the sliding occurs between two tungsten monolayers where eventually atomic jamming events are observed. While the jamming events trigger the nucleation of dislocations within the W specimen, significant amorphization at the sliding interface and within the WC sample is also observed. The amorphization process typically initiates at the sliding interfaces and sometimes propagates into the bulk of the WC specimen. The degree of amorphization along the height of the W-WC tribocouple is shown in Figure 7 at a shearing time of 1000 ps.

3.2. Lubricated Sliding. *3.2.1. Friction and Wear Behavior.* Figure 8 (a) shows the friction coefficient vs the number of cycles for the WC/W tribocouple with hexadecane as a lubricant and sliding velocities ranging from 0.2 to 20 mm/s. It is observed that the coefficient of friction is similar for all sliding velocities. At the onset of the experiment, the friction coefficient is approximately 0.1 but increases within the

dx.doi.org/10.1021/am4010094 | ACS Appl. Mater. Interfaces 2013, 5, 6123−6135

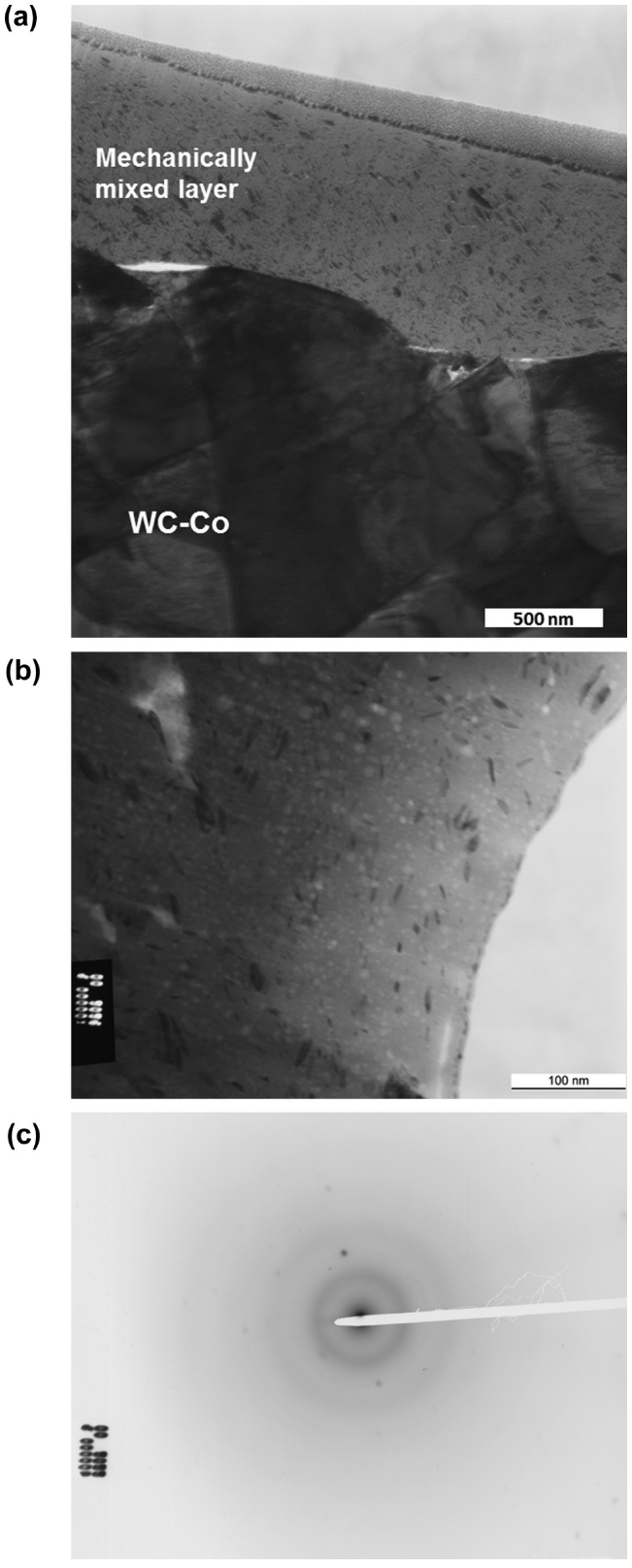

Figure 5. Cross sectional TEM images of (a) the worn counterface (WC) of the dry test in the parallel direction to the sliding, (b) the mechanically mixed layer, and (c) the selected area electron diffraction pattern revealing an amorphous and/or nanocrystalline structure.

first 50 cycles to 0.15. Subsequently, it decreases slightly over 40 cycles and remains nearly constant at 0.1. Sliding experiments for 5000 cycles are also performed (not presented here) and reveal that the friction coefficient remains constant at 0.1 for longer periods.

A somewhat different behavior of the coefficient of friction is observed with the evolution of the wear rate. The wear rate (i.e., depth/sliding distance) vs cycles for the experiment with a 5 mm/s sliding velocity is shown in Figure 9. Initially, the wear rate is slightly above 100 nm/m and decreases below 40 nm/m over 80 cycles. The wear rate at the end of the experiments (i.e., measured ex situ with a confocal microscope) is approximately 5 nm/m. For comparison the wear rate at the end of the dry test is also plotted in this figure (black triangle, data taken from ref 33) and is by a factor of 10 higher compared to the value of the lubricated experiment.

3.2.2. 'Online' Analysis of the Surface Topography. DHM images obtained throughout the lubricated experiments are shown in Figure 8 (b) for cycles 10, 100, 250, 300, and 400. Within the first few cycles, few grooves (i.e., scratches) parallel to the sliding direction are created on the W surface, as observed in the image of the 10th cycle. Upon further sliding, more grooves are visible, and the wear track is wider. By the 400th cycle, debris particles are present on the wear track. Observations of individual particles from consecutive images indicate that the particles are mobile and float within the hexadecane, as shown in Figure 10.

Similar observations are also seen with the roughness measurements parallel and perpendicular to the sliding direction, Figure 11. While the roughness in the parallel direction remains low, the average roughness in the perpendicular direction increases within the first few cycles of the experiment. The roughness in the perpendicular direction continues to increase upon further sliding and remains higher compared to the roughness in the parallel direction. The R_a value in the parallel direction shows a slight increase after the 100th cycle; however, the roughness measured ex situ is comparable to the values at the beginning of the experiment. This indicates that the increase in the roughness is rather due to particles than due to surface roughening. The roughness in the perpendicular direction (i.e., measured ex situ), on the other hand, is slightly higher compared to the value obtained from the DHM microscope near the end of the experiment.

3.2.3. Third-Body Behavior. SEM image and XPS chemical state maps of the counterface before and after different sputter times are shown in Figure 12. Analysis of the individual elements reveals a high carbon concentration, bound in organic aliphatic hydrocarbons, covering the complete tungsten carbide surface with small contributions of oxygen. In addition, slightly lower tungsten concentrations of tungsten oxide (W4f oxide) as well as tungsten carbide (W4f metal plus carbide) are detected directly on the surface. After short sputtering (i.e., 125 s), the organic carbon layer decreases significantly with the exception of one spot where local lubricant residuals are still present. Concurrently, the carbide (i.e., the C1s carbide map) and the tungsten concentrations (i.e., the W4f metal plus carbide map) increase. The tungsten oxide, on the other hand, decreases according to the O1s oxide maps during the first sputter step. The slower decrease in comparison to the carbon signal indicates a pronounced tungsten oxide layer. The corresponding tungsten W4f oxide map shows a slight different behavior at the surface; the map at the surface reveals lower tungsten (W4f oxide) concentration in comparison to the maps after 125 and 400 s of sputtering. This is a clue of a higher oxidation state underneath the surface, e.g. WO_3 instead of WO_2 at the surface.

dx.doi.org/10.1021/am4010094 | ACS Appl. Mater. Interfaces 2013, 5, 6123−6135

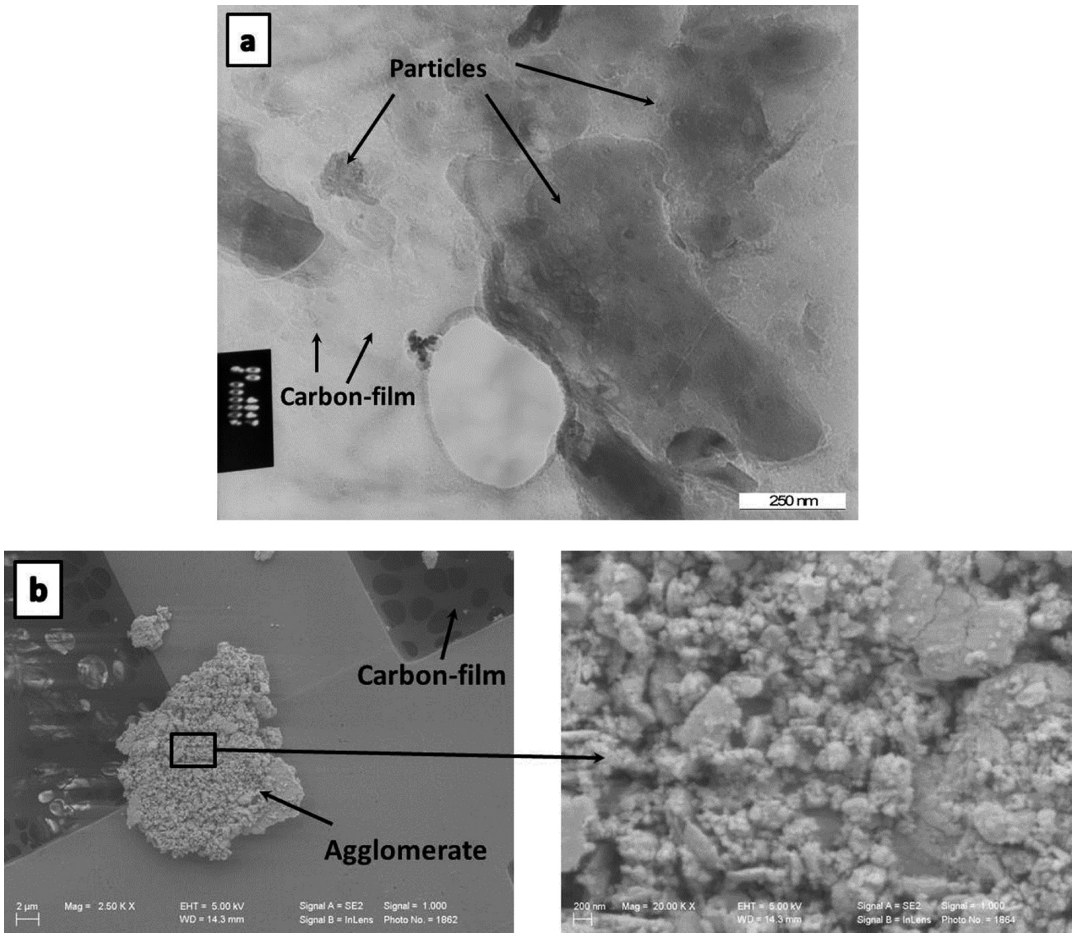

Figure 6. (a) TEM images of debris particles. Debris particles consist of various shapes and sizes; the size ranges anywhere from a few nanometers to several micrometers. (b) SEM image of agglomerate consisting of nanometer sized globular and μm-sized flakelike debris particles.

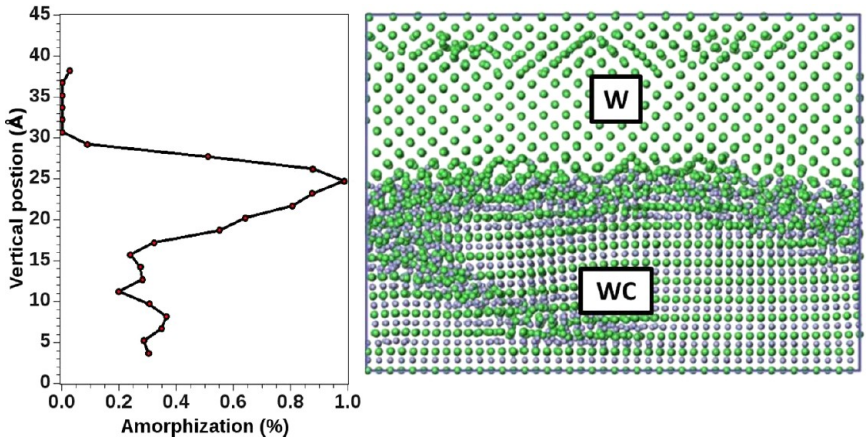

Figure 7. Degree of amorphization along the height of the W-WC tribocouple in a flat-on-flat MD simulation after sliding for 1000 ps. The corresponding simulation is shown in the right panel. The evolution of the amorphization with respect to the sliding distance is shown in ref 33.

Thickness of the oxide film in the lubricated case, however, is much smaller in comparison to the dry case.

Ex situ analysis of the tungsten surface reveals a slightly different behavior, Figure 13. While some carbon is detected near the surface, the atomic concentration decreases nearly to zero up to a sputtering depth of 10 nm (i.e., 5 min sputtering time). Similarly, a small concentration of carbide is observed only with sputter depth below 20 nm. More interestingly, the tungsten concentration is slightly lower for sputter depth below 60 nm when compared to the unworn surface.[33] Contrarily, the oxygen content below 60 nm of sputtering depth is higher compared to the unworn surface.

Cross sectional SEM images of the worn W and WC surfaces are combined in Figure 14. As shown with the SEM image in Figure 12, some mechanical mixing is observed on the WC surface. This layer is present not only on the surface but also partly within the valleys (i.e., holes) of the WC. More interestingly, similarly to the dry sliding experiments, no

dx.doi.org/10.1021/am4010094 | ACS Appl. Mater. Interfaces 2013, 5, 6123−6135

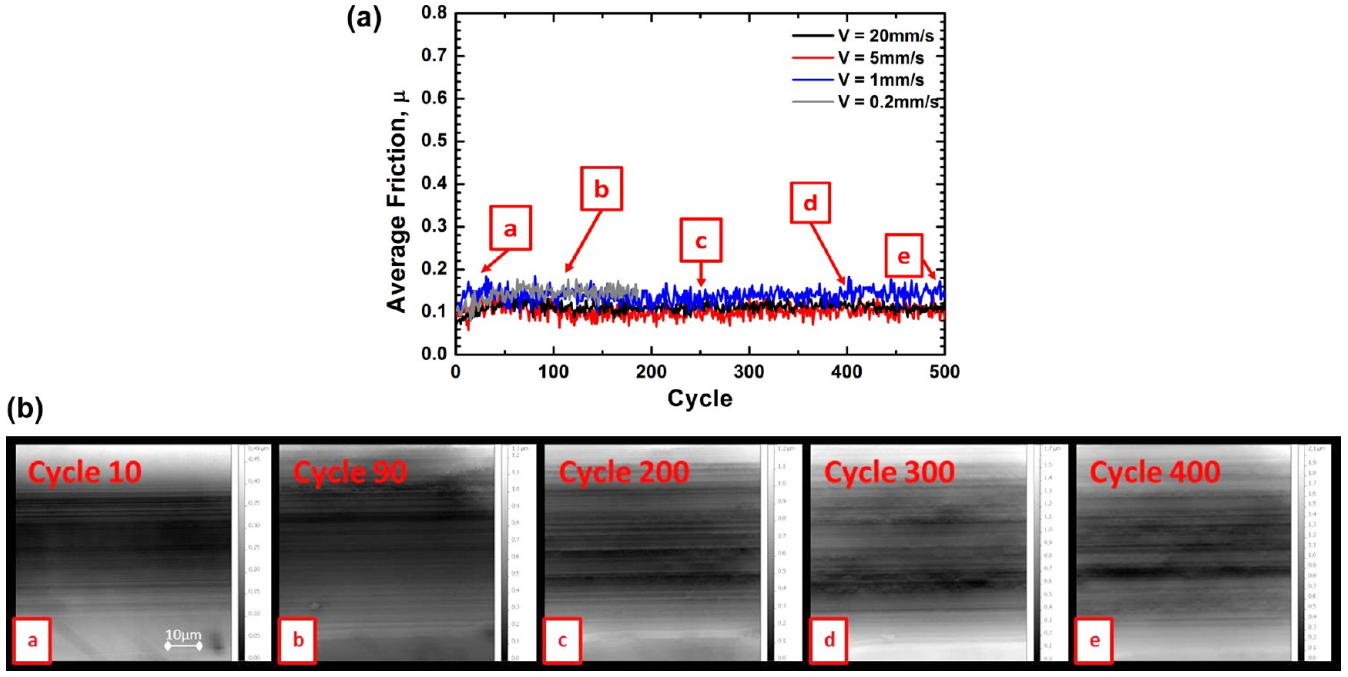

Figure 8. (a) Friction coefficients vs cycle for lubricated sliding using sliding velocities of 0.2, 1, 5, and 20 mm/s. The error in the coefficient of friction between two experiments with the same sliding conditions is less than 0.02. (b) DHM images are obtained using the 'online' tribometer and are shown below the plot for v = 5 mm/s.

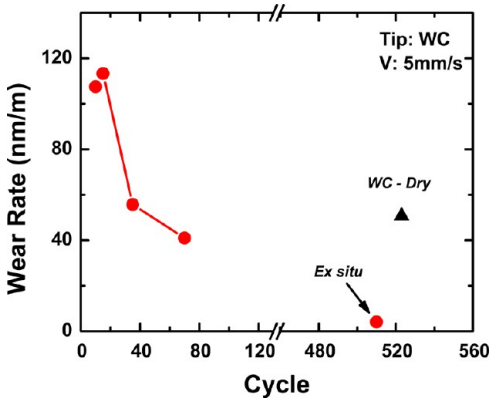

Figure 9. Wear rate (i.e., depth/sliding distance) vs cycle for the lubricated case using a sliding velocity of 5 mm/s. Due to the large wear track created with the WC tip, wear rates are only possible to be obtained up to the 70th cycle. The last data point of the wear rate for the dry and lubricated test is also included and obtained using ex situ confocal microscopy.

apparent structure is observed within this layer. The lower image shows the W surface, which reveals a thin grain refined layer near the surface without a sharp transition line to the underlying material.

Auger electron spectroscopy (AES) analysis of the debris particles is shown in Figure 15. In addition to a high carbon concentration (i.e. ~70 At %), the elemental analysis reveals oxygen and tungsten. The line shape of the carbon auger peak is similar to carbon of organic layers and reveals no graphite shoulder and no double structure like carbide in the differentiated signal. The high carbon concentration is a preliminary clue that chemical reaction occurred between the debris particles and the hexadecane. However, it should be noted that a small contribution of tungsten carbide particles may remain hidden under the carbon signal of aliphatic carbon and thus should not be excluded completely.

3.2.4. Atomistic Simulations of Lubricated Contact. W vs WC nanotribocouples with atomically rough lubricated (with hexadecane) interfaces are constructed in order to understand the underlying mechanism of the third-body formation. Snapshots of the contact interface evolution in the simulations are shown in Figure 16 for sliding times of 0, 71, 400, and 1200 ps. Upon initial sliding the WC surface breaks down the nanoasperity of the W surface (i.e., ploughs through the W). While most W atoms from the broken asperities become mobile in-between the interfaces, few W atoms bond to the WC surface. At that point, the hexadecane has not yet completely covered the contact between the WC and the W surface. However, upon further sliding, the W surface is nearly flattened by the WC specimen, and the contact is completely covered by the hexadecane monolayer. Interestingly the loose W atoms from the W surface become trapped in the valley of the WC surface and are mixed in with the hexadecane. For this simulation we obtain a shear stress of 1.3 GPa, whereas a corresponding simulation without the lubricant yields a value of 4.7 GPa. Thus, even a small amount of lubricant significantly reduces the force required to slide the system.

4. DISCUSSION

'Online' macroscopic tribometry along with ex situ X-ray photoelectron spectroscopy, transmission electron microscopy, and cross-sectional focused ion beam analysis as well as molecular dynamics simulations are linked together in this study in order to provide a better understanding of the third-body formation process in metallic contacts. While we use a WC/W tribocouple as an example, the trends in lubricated (i.e., base lubricant) and dry conditions for this system should translate onto other metallic sliding contacts as well. The tribological experiments show that dry sliding of WC against W results in higher friction

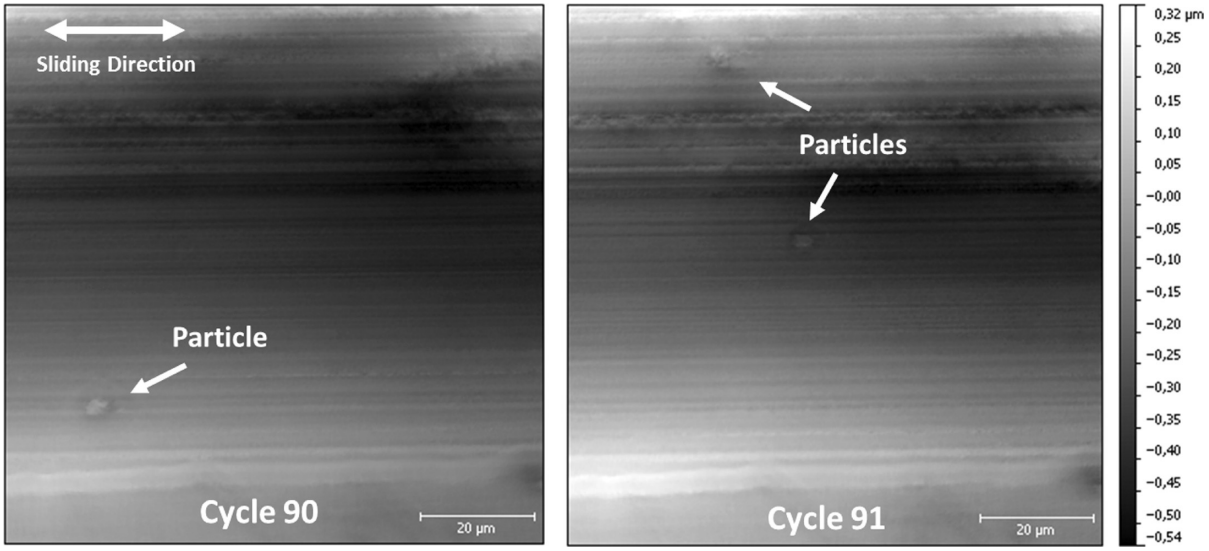

Figure 10. DHM images of two consecutive cycles (i.e., cycles 90 and 91) for a sliding velocity of 5 mm/s. Observations of individual particles indicate that the particles are mobile and float within the hexadecane.

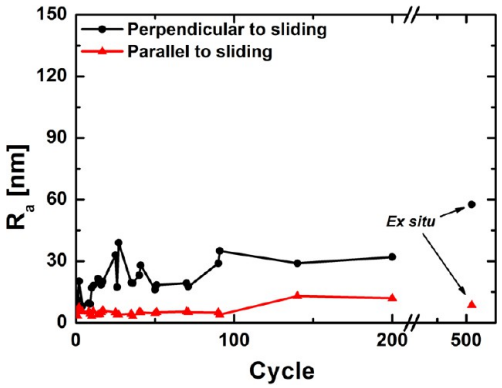

Figure 11. Roughness values obtained using a thin rectangle parallel to the sliding direction and a thin rectangle perpendicular to the sliding direction for the experiments performed with hexadecane as a lubricant and a velocity of 5 mm/s.

values compared to lubricated conditions. The 'online' analysis of the wear track correlates well with the friction behavior; roughness values follow the trend in the friction coefficient closely for both conditions, while higher roughness is observed with the dry conditions compared to lubricated sliding. Subsequently to the increase in average roughness of the wear track (i.e., acquired on a square area), in the case of dry sliding, an increase in the coefficient of friction is observed. In addition, the higher scatter in the roughness values, after the initial increase, correlated with the higher scatter in the friction. While an initial increase in the roughness for the lubricated condition is also observed, the values remain lower compared to the dry experiment for all cycles. Consequently, a lower friction power density is dissipated that in turn may influence the evolution of topography and third-body.

To better understand the topographical behavior and to gain further insights on the velocity accommodation modes of both sliding regimes, the evolution of the roughness is explored in the parallel and the perpendicular direction to the sliding. For dry sliding conditions, the average roughness in the perpendicular direction increases instantaneously after the first few cycles, while the roughness values in the parallel direction initially remain low. This behavior indicates the formation of grooves and scratches along the sliding direction, which are also noticed in the topography images (see Figure 1b). The formation of such a morphology has been previously referred to as an adaptation of the surface topographies between the sliding interfaces.[1] These types of adaptation process typically consist of plowing or cutting events caused by the asperities of the harder material (in this study the WC counterface) onto the softer one.

These observations are consistent with the interpretation of the rough-on-rough atomistic simulations without hexadecane as a lubricant.[33] The rough WC surface plows through the tungsten asperities immediately upon the initial sliding. Consequently, the tungsten surface becomes disordered and sliding occurs on a nanocrystalline tungsten layer. Therefore, this confirms qualitatively the initial assumption of the tendency of the adaptation process within the first few cycles, which is based on the roughness measurements in the perpendicular direction to the sliding.

The increase in roughness for the parallel direction in the dry sliding test occurs at higher cycle numbers, compared to the perpendicular direction, and is identical to the increase in the friction coefficient. The roughness behavior parallel to the sliding indicates the initiation of an additional shear accommodation mode between the WC and W surfaces, which causes a nearly instantaneous increase in the coefficient of friction. Based on the ex situ analysis of the cross sections, it is suggested that this shear accommodation consists of mechanical mixing between the two surfaces and mechanical deformation of the tungsten surface resulting in grain refinement up to approximately 700 nm below the surface. Such near-surface grain refinement due to tangential forces is typical for metallic friction and is often accounted for by the rotation of clusters of atoms[10,13] or ratchetting under multiaxial shear fatigue.[15] Still, the acting mechanisms of how the friction power is dissipated are not fully understood and are a matter of further study. In addition, XPS analysis shows an increased concentration of oxygen within at least 180 nm below the surface, which is also consistent with literature on metallic friction.[36] Yet the final experimental evidence for crystalline material is still missing. An investigation in a single-contact

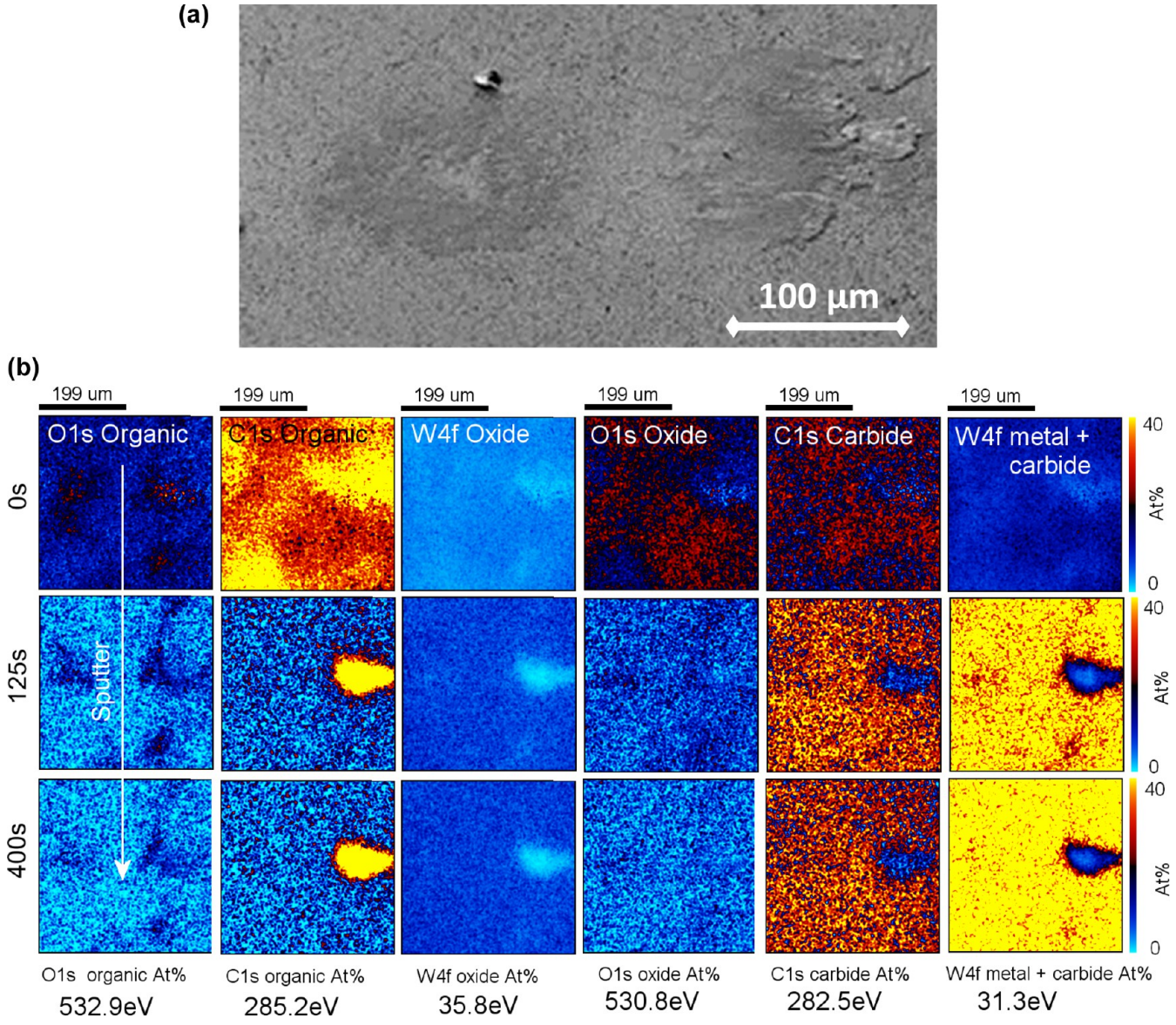

Figure 12. (a) SEM image (SE, 10 kV, 300×) of the worn tungsten- carbide counterface (i.e., v = 20 mm/s) and (b) XPS chemical state maps of the same counterface for different binding states of oxygen, tungsten, and carbon under lubricated sliding conditions, without sputtering (1st row), after sputtering for 125 s (2nd row), and after sputtering for 400 s (3rd row) with 2 keVAr^+. For each element two different binding states are presented with the binding states and corresponding photoelectron peak energies for the different binding states written at the bottom of the diagram. All maps are quantified in atomic concentrations.

setup proposed a mechanical instability criterion for the spontaneous grain refinement and the sharp interface between the refined and the "undisturbed" substrate material, which corresponds to Johnson's cavity criterion.[37] Certainly this type of deformation and mixing can evolve in the generation of wear debris on the surface. This would agree quite well with the increase in roughness parallel to the sliding as well as with the particle analysis, which reveals the presence of tungsten carbides and tungsten oxides debris particles. In addition, the formation of debris particles with the increase in friction is also observed with the topography images, Figure 1 (b). While few particles are stationary on the wear track, the images reveal that most particles moved around throughout the sliding. The development or detachment of debris particles onto the wear track could have also originated from the entry zone and the nanocrystalline and/or amorphous layer (i.e., internal zone), which are observed ex situ on the counterface. The higher roughness

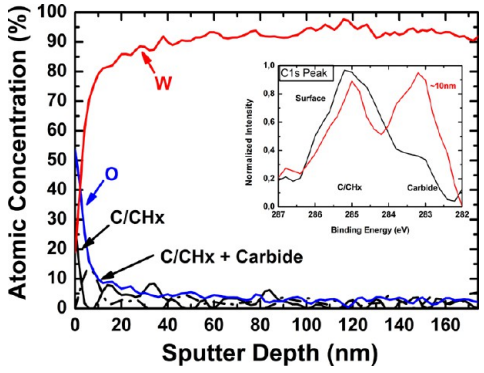

Figure 13. XPS analysis of the worn tungsten under lubricated sliding conditions. The sputtering depth (i.e., *x*-axis) is estimated based on depth calibrations with SiO_2; a sputtering time of 10 min can be estimated to be approximately 20 to 30 nm.

dx.doi.org/10.1021/am4010094 | ACS Appl. Mater. Interfaces 2013, 5, 6123−6135

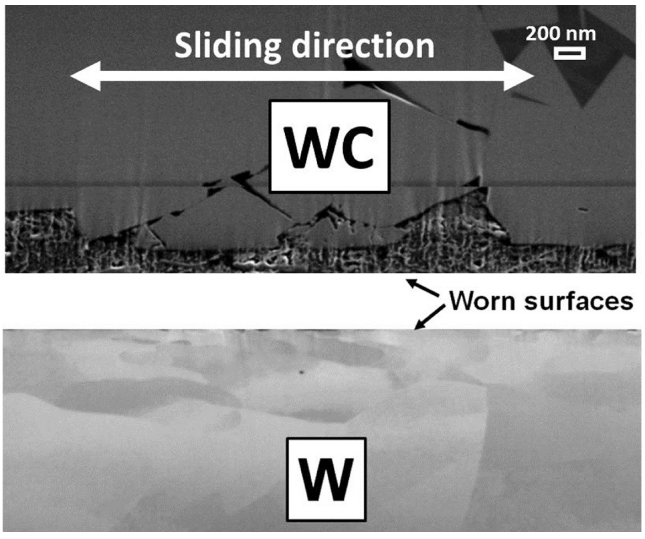

Figure 14. Composition of cross sectional SEM images (SE), produced by separate FIB cuts, of the worn surface (W) and counterface (WC) of the lubricated test (v = 5 mm/s) in the parallel direction to the sliding.

values of the entry zone on the counterface could be an indication that it is composed of debris particles, which are collected from these loose particles on the wear track and then get redeposited through the sliding.

Elemental analysis for dry sliding of the internal zone reveals a higher tungsten concentration near the surface with an increased carbide concentration in the subsurface region. This indicates that in addition to tungsten/tungsten oxide transferring onto the WC tip, a mixing event occurs between both materials resulting in a mechanically mixed layer as observed in Figure 5. Similarly, the near surface region of the wear track (i.e., the tungsten plate) does not contain any carbide or cobalt concentration with a dominant tungsten concentration. In addition to the increased tungsten concentration on the surfaces of both interfaces, an increase in oxygen is also observed. Therefore, sliding takes place between ultrafine crystalline and mechanically mixed tungsten layers with oxides being blended into the third bodies.[38] Despite the lack of oxygen in the computer model, this behavior correlates well with our observations of the W/WC atomistic simulations.[33] We have previously reported that the exposed carbide layer of the WC surface creates a strong bond with the first W monolayer of the counterface (i.e., the W sample) upon initial sliding. Subsequently, sliding takes place between two W layers, as also observed with the XPS analysis. Upon further sliding, jamming events within the W specimen are observed, resulting in nucleation of dislocations. In addition, significant amorphization is observed within the tungsten-carbide, which is also consistent with the TEM analysis of the counterface, Figure 5. It is certainly true that environmental conditions can have an effect on the tribological performance, making a direct comparison between experiments and simulations somewhat

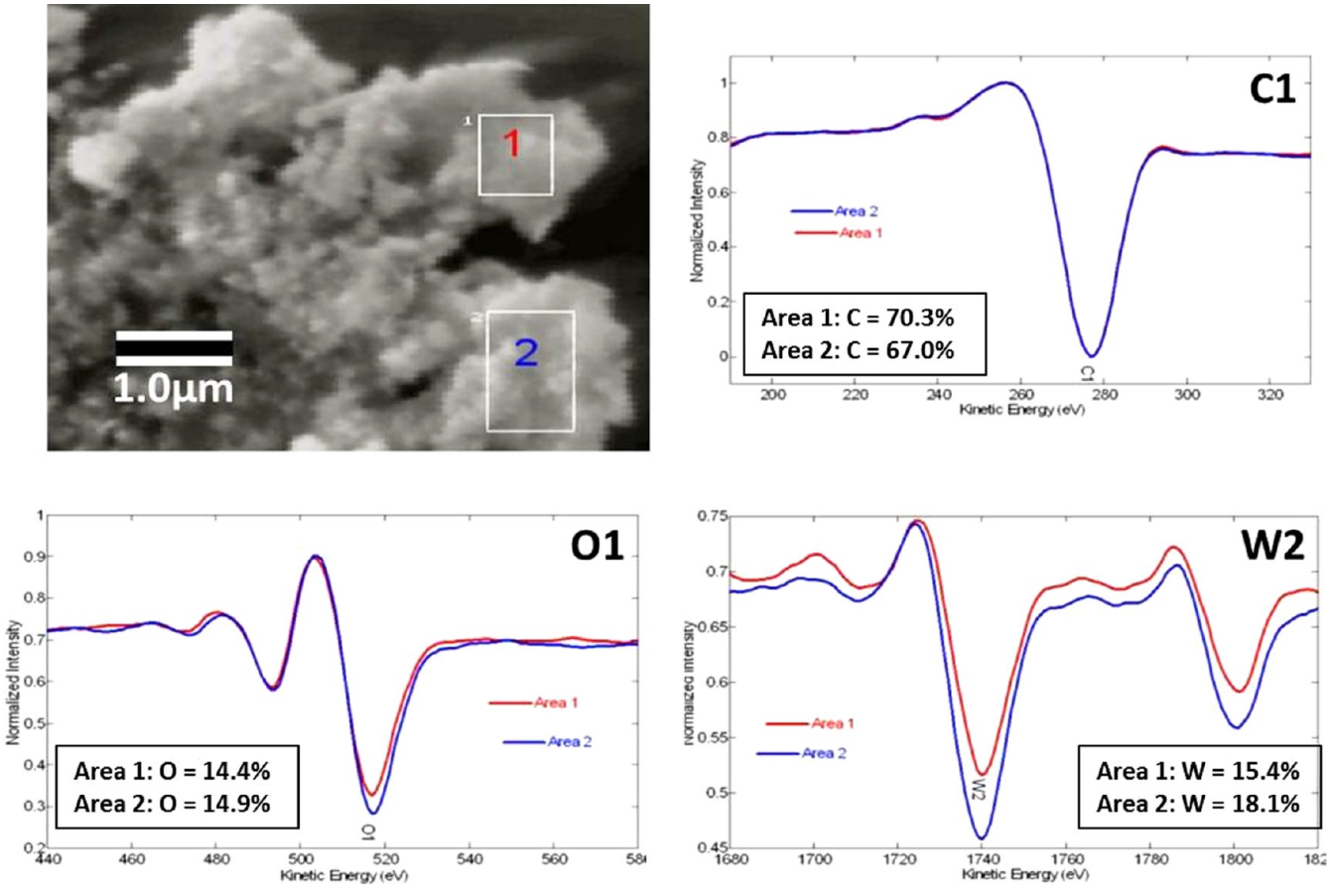

Figure 15. AES analysis of a debris particle obtained from the lubricated sliding test (i.e., 20 mm/s). In addition to a high carbon concentration, the elemental analysis reveals oxygen and tungsten.

dx.doi.org/10.1021/am4010094 | ACS Appl. Mater. Interfaces 2013, 5, 6123−6135

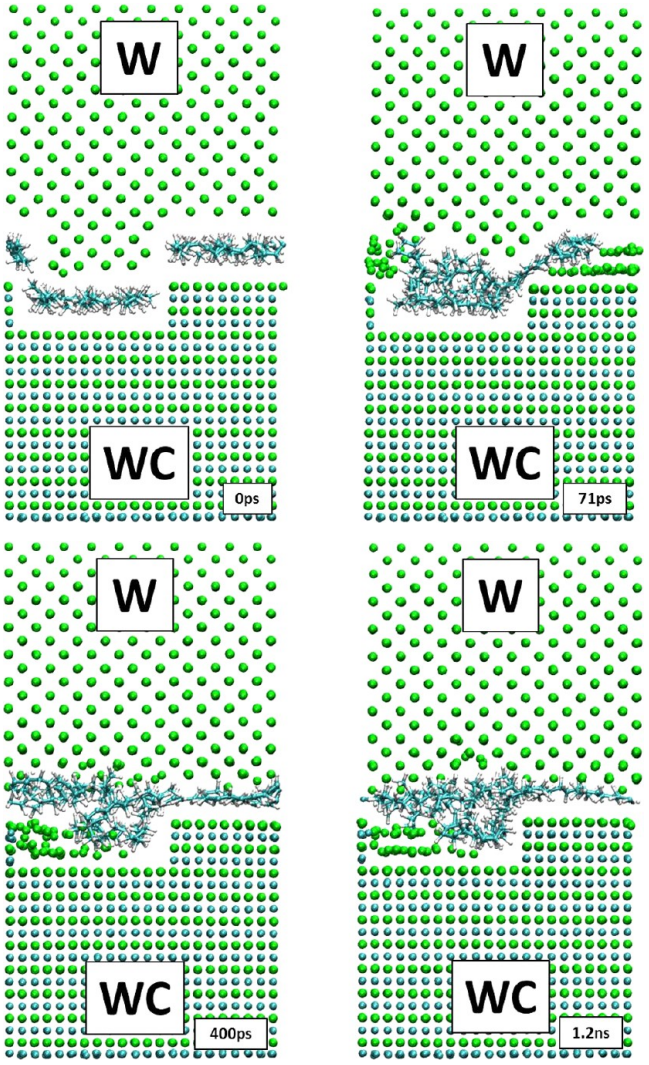

Figure 16. Atomistic simulation of a W/WC rough on rough sliding couple with a 5 GPa normal pressure and a 50 m/s sliding velocity. Snapshots of the evolution in the simulations are taken for a sliding time of 0, 71, 400, and 1200 ps.

questionable. However, we have resolved this issue in our previous study[33] by performing experiments in ultrahigh vacuum of a WC sliding against W, which displayed a similar behavior to the tests in air. Therefore, the enrichment of oxygen in the near surface region for the tests in air does not have an influence on the friction behavior.[33]

Similarly to dry sliding, the topography images for the lubricated sliding condition reveal grooves parallel to the sliding direction within the first few cycles. In addition, the roughness in the perpendicular direction increases at a high rate within the first few cycle, while the roughness parallel to the sliding remains low and constant indicating initial adaptation (i.e., plowing events) of the surfaces. These plowing events are also consistent with the observations of the simulations with a hexadecane monolayer in-between the sliding interfaces; upon initial sliding, the WC surface comes into contact with the W nanoasperity, without the lubricant in-between, causing plowing of the WC on the W surface. Upon further sliding, the W nanoasperity is completely broken down and the W surface is nearly flat. While some of the atoms, that initially constructed this W asperity, bond to the WC surface, most of them get pushed and trapped into the valley/hole of the WC surface. Subsequently, the W atoms remain within this valley for the rest of the simulation where they get mixed-in with the hexadecane. These observations are consistent with the ex situ analysis of the surfaces in Figure 14; a thin mixed layer is observed on the counterface, which fills up all cavities on the WC surface and consists mostly of tungsten, carbon, and − in the laboratory experiment − oxygen near the surface.

Further ex situ analysis of the worn surfaces shows that the lubricated sliding results in a less pronounced third-body formation compared to dry sliding; while a thin mixed layer is observed on the WC counterface, only slight grain refinement is evident in the near surface region of the W specimen. Similarly, XPS analysis of the W surface reveals a less pronounced increase in the oxygen content compared to dry sliding. This behavior is also confirmed with the simulations, where no severe amorphization and/or nucleations of dislocations are observed within the tungsten carbide specimen as seen with the dry sliding experiments. One possible explanation of the less evident third-body formation for lubricated sliding (i.e., mechanically mixed layer on the WC counterface and grain-refined layer on the W surface) is that the lubricant restricts the bonding between the two interfaces leading to less transfer. Subsequently, fewer atomic jamming events occur hindering the nucleation of dislocation and thus the formation of a grain refined layer. A less likely reason for the reduced third-body formation in the lubricated sliding condition is the difference in the real contact pressure within the two systems; the cavities (i.e., holes) of the WC counterface are filled up with a mixture of tungsten and carbon, which increases the contact area and therefore decrease the contact pressure. Consequently, the lower contact pressure in the lubricated condition leads to less severe plastic deformation and reduces the nucleation of dislocation within the W sample resulting in a less pronounced grain-refined layer.

In terms of the friction behavior, during the initial adaptation events (i.e., running-in stage), the coefficient of friction in the lubricated case is similar to the one of dry sliding. However, upon further sliding, the coefficient of friction increases drastically for dry sliding but remains low for the lubricated case. This behavior can be explained by differences in velocity accommodation modes during the steady state sliding. In the case of dry experiments the sliding motion is accommodated by amorphization of the counterface. When hexadecane is present, however, MD simulations reveal that after the initial plowing events of the WC tip, sliding occurs on monolayers of the lubricant, which results in low friction values due to the low viscosity of hexadecane.

5. CONCLUSION

Macroscopic tribometry shows that dry sliding of WC against W results in higher friction values compared to lubricated conditions. The 'online' analysis of the wear track correlates well with the friction behavior; roughness values closely follow the trend of the friction coefficient for both conditions with higher roughness being observed for the dry conditions relative to the lubricated conditions. To gain further insights on the velocity accommodation modes of both sliding regimes, the evolution of the roughness is explored in the parallel and the perpendicular direction to the sliding. This analysis reveals plowing events of the WC surface onto the W surface during the initial stage of the sliding for dry and lubricated conditions.

dx.doi.org/10.1021/am4010094 | ACS Appl. Mater. Interfaces 2013, 5, 6123−6135

Classical molecular dynamics simulations of W sliding against WC (i.e., with and without hexadecane) with rough surfaces are consistent with these observations.

Ex situ analysis for the dry tests reveals the formation of a grain refined layer in the near surface region of the tungsten specimen and an amorphous layer on the WC counterface. These observations indicate that subsequently to the initial plowing events, the sliding occurs mainly within an amorphized WC layer, as also confirmed by MD simulations. The lubricated sliding, on the other hand, results in a less pronounced third-body formation; while a thin mixed layer is observed on the WC counterface, only slight grain refinement is evident in the near surface region of the W specimen. Similarly to the dry sliding, these ex situ analyses are consistent with atomistic simulations; following the initial adjustment of the two surfaces (i.e., plowing events of the WC surface), the sliding occurs on monolayers of the lubricant, which results in low friction values due to the low viscosity of hexadecane. The lubricant restricts the contact between the two surfaces resulting in nearly no nucleation of dislocations or mechanical mixing events.

AUTHOR INFORMATION

Corresponding Author

*E-mail: pantcho.stoyanov@mail.mcgill.ca.

Notes

The authors declare no competing financial interest.

ACKNOWLEDGMENTS

We thank the Deutsche Forschungsgemeinschaft for financial support under contracts FI451, MO879, and SCH425. T.J. acknowledges support from the Academy of Finland (project number 136165). The authors would also like to thank Diego Marchetto and Eberhard Nold for their help with the XPS depth profiles investigations on the PHI 5000 VersaProbe.

REFERENCES

(1) Descartes, S.; Berthier, Y. *Wear* **2002**, *252*, 546−556.
(2) Berthier, Y.; Godet, M.; Brendle, M. *Tribol. Trans.* **1989**, *32*, 490−496.
(3) In *Fundamentals of Friction: Macroscopic and Microscopic Processes*; Pollock, H. M., Singer, I. L., Eds.; Netherlands, 1992; pp 237−261.
(4) Singer, I. L.; Dvorak, S. D.; Wahl, K. J.; Scharf, T. W. *J. Vac. Sci. Technol., A* **2003**, *21*, S232−S240.
(5) Scharf, T. W.; Singer, I. L. *Tribol. Lett.* **2003**, *14*, 137−145.
(6) Chromik, R. R.; Winfrey, A. L.; Luning, J.; Nemanich, R. J.; Wahl, K. J. *Wear* **2008**, *265*, 477−489.
(7) Kathryn, W. Macroscale to Microscale Tribology. In *Micro- and Nanoscale Phenomena in Tribology*; CRC Press: 2011; pp 5−22.
(8) Stoyanov, P.; Gupta, S.; Lince, J. R.; Chromik, R. R. *Tribol. Int.* **2012**, *52*, 144−152.
(9) Hanke, S.; Samerski, I.; Schöfer, J.; Fischer, A. *Wear* **2009**, *267*, 1319−1324.
(10) Fischer, A. *Comput. Mater. Sci.* **2009**, *46*, 586−590.
(11) Dienwiebel, M.; Pöhlmann, K.; Scherge, M. *Tribol. Int.* **2007**, *40*, 1597−1602.
(12) Godet, M. *Wear* **1984**, *100*, 437−452.
(13) Rigney, D. A. *Wear* **2000**, *245*, 1−9.
(14) Shockley, J. M.; Strauss, H. W.; Chromik, R. R.; Brodusch, N.; Gauvin, R.; Irissou, E.; Legoux, J.-G. *Surf. Coat. Technol.* **2012**, *215*, 350−356.
(15) Fischer, A.; Weiß, S.; Wimmer, M. A. *J. Mech. Behav. Biomed. Mater.* **2012**, *9*, 50−62.
(16) Prasad, S. V.; Battaile, C. C.; Kotula, P. G. *Scr. Mater.* **2011**, *64*, 729−732.
(17) Battaile, C. C.; Boyce, B. L.; Weinberger, C. R.; Prasad, S. V.; Michael, J. R.; Clark, B. G. *Acta Mater.* **2012**, *60*, 1712−1720.
(18) Sriraman, K. R.; Strauss, H. W.; Brahimi, S.; Chromik, R. R.; Szpunar, J. A.; Osborne, J. H.; Yue, S. *Tribol. Int.* **2012**, *56*, 107−120.
(19) Dvorak, S. D.; Wahl, K. J.; Singer, I. L. *Tribol. Trans.* **2002**, *45*, 354−362.
(20) Sawyer, W. G.; Wahl, K. J. *MRS Bull.* **2008**, *33*, 1145−1150.
(21) Wahl, K. J.; Chromik, R. R.; Lee, G. Y. *Wear* **2008**, *264*, 731−736.
(22) Singer, I. L.; Dvorak, S. D.; Wahl, K. J.; Scharf, T. W. In *Tribology Series*; Dowson, D., Priest, M., Dalmaz, G., Lubrecht, A. A., Eds.; 2002; Vol. *40*, pp 327−336.
(23) Strauss, H. W.; Chromik, R. R.; Hassani, S.; Klemberg-Sapieha, J. E. *Wear* **2011**, *272*, 133−148.
(24) Chromik, R. R.; Baker, C. C.; Voevodin, A. A.; Wahl, K. J. *Wear* **2007**, *262*, 1239−1252.
(25) Stoyanov, P.; Strauss, H.; Chromik, R. R. *Wear* **2012**, *274*−*275*, 149−161.
(26) Dvorak, S. D.; Wahl, K. J.; Singer, I. L. *Tribol. Lett.* **2007**, *28*, 263−274.
(27) Scharf, T. W.; Singer, I. L. *Tribol. Trans.* **2002**, *45*, 363−371.
(28) Fu, X.-Y.; Falk, M. L.; Rigney, D. A. *Wear* **2001**, *250*, 420−430.
(29) Karthikeyan, S.; Kim, H. J.; Rigney, D. A. *Phys. Rev. Lett.* **2005**, *95*, 106001.
(30) Kim, H. J.; Emge, A.; Winter, R. E.; Keightley, P. T.; Kim, W. K.; Falk, M. L.; Rigney, D. A. *Acta Mater.* **2009**, *57*, 5270−5282.
(31) Juslin, N.; Erhart, P.; Traskelin, P.; Nord, J.; Henriksson, K. O. E.; Nordlund, K.; Salonen, E.; Albe, K. *J. Appl. Phys.* **2005**, *98*, 123520.
(32) Pastewka, L.; Pou, P.; Pérez, R.; Gumbsch, P.; Moseler, M. *Phys. Rev. B: Condens. Matter Mater. Phys.* **2008**, *78*, 161402.
(33) Stoyanov, P.; Romero, P. A.; Järvi, T. T.; Pastewka, L.; Scherge, M.; Stemmer, P.; Fischer, A.; Dienwiebel, M.; Moseler, M. *Tribol. Lett.* **2013**, *50*, 67−80.
(34) Korres, S.; Dienwiebel, M. AIP: 2010; Vol. *81*, p 063904.
(35) Pastewka, L.; Moser, S.; Moseler, M. *Tribol. Lett.* **2010**, *39*, 49−61.
(36) Wilson, R. *Proc. R. Soc. London, Ser. B* **1952**, *212*, 450−452.
(37) Prasad, S. V.; Michael, J. R.; Majumdar, B. S.; Battaile, C. C.; Moody, N. R.; Cordill, M. J.; Jungk, J. M.; Bammann, D. J. Sandia National Laboratories: Albuquerque and Livermore, 2006; p 69.
(38) Fu, X.-Y.; Rigney, D. A.; Falk, M. L. *J. Non-Cryst. Solids* **2003**, *317*, 206−214.